

## Model for erosion-deposition patterns

D. O. Maionchi,<sup>1,2</sup> A. F. Morais,<sup>1</sup> R. N. Costa Filho,<sup>1,3</sup> J. S. Andrade, Jr.,<sup>1,4</sup> and H. J. Herrmann<sup>1,4</sup>

<sup>1</sup>*Departamento de Física, Universidade Federal de Ceará, 60451-970 Fortaleza-Ceará, Brazil*

<sup>2</sup>*Institut für Computerphysik, Universität Stuttgart, Pfaffenwaldring 27, 70569 Stuttgart, Germany*

<sup>3</sup>*The Abdus Salam International Centre for Theoretical Physics, Strada Costiera 11, 34014 Trieste, Italy*

<sup>4</sup>*Computational Physics, IfB, ETH Hönggerberg, HIF E 12, CH-8093 Zürich, Switzerland*

(Received 5 December 2007; revised manuscript received 15 April 2008; published 10 June 2008)

We investigate through computational simulations with a pore network model the formation of patterns caused by erosion-deposition mechanisms. In this model, the geometry of the pore space changes dynamically as a consequence of the coupling between the fluid flow and the movement of particles due to local drag forces. Our results for this irreversible process show that the model is able to reproduce typical natural patterns caused by well-known erosion processes. Moreover, we observe that, within a certain range of porosity values, the grains form clusters that are tilted with respect to the horizontal with a characteristic angle. We compare our results to recent experiments for granular material in flowing water and show that they present a satisfactory agreement.

DOI: [10.1103/PhysRevE.77.061402](https://doi.org/10.1103/PhysRevE.77.061402)

PACS number(s): 82.33.Ln, 45.70.Qj, 47.57.Gc, 47.56.+r

### I. INTRODUCTION

Nature preservation and environmental protection are important issues on the agendas of governments and nongovernmental organizations. Consequently, these issues have been the subject of intense study, where the main concern is to understand how the actions of human beings affect the environment. For example, deforestation and pollutant emissions are related to climate changes resulting in floods and erosion. In particular, erosion can be responsible for diminishing the quality of life, because it affects the soil, causing a negative impact on the economy. Aside from its economic and ecological aspects, the erosion problem also attracts the interest of geologists and physicists. In geology, this is an extremely rich area as many of the patterns observed in nature stem from erosion or deposition processes. In physics, the formation of such patterns spans a huge range of spatial and temporal scales. This pattern formation process is directly related to the transport of solid granular particles via a fluid and presents a rich phenomenology along with a variety of applications [1,2]. Particular applications are fractal river basins [3], meandering rivers [4], dune fields [5,6], granular avalanches [7,8], and ripple marks [9] on sandbanks or on coastal continental platforms.

It is difficult to provide a fully consistent description of particle-laden flows from either a one- or two-phase point of view. Most of the practical knowledge of erosion comes from empirical laws often derived from field measurements. This has provoked interest in theoretical descriptions of these systems [10–12] and visualization of them in computational simulations. Several attempts to understand the dynamics of river basin formation from the statistical physics point of view have been made recently, but many questions are raised when one tries to relate basic transport properties to large-scale pattern-forming instabilities [13]. A fundamental open question is the following: How do objects made of granular materials respond to the action of external factors? Many experiments [14–21] have been performed in the last few years to answer this question. For example, in Fig. 1, we see

a laboratory-scale experiment which reproduces a rich variety of natural patterns with few control parameters [14]. These patterns are characterized by chevron alignments, which means that the paths created by the fluid present a characteristic branching angle that depends on the parameters varied in the experiment.

In this paper, we investigate through numerical simulation a physical model that is designed to represent the generic situation of flowing water on a plane composed of an erodible sediment layer. This occurs naturally when the sea retreats from the shore or when a reservoir is drained. The flow of granular materials on planes is also of interest within the context of both industrial processing of powders and geophysical instabilities such as landslides and avalanches. These flows have been found to be complex, exhibiting several different flow regimes as well as particle segregation effects and instabilities [22]. This paper is organized as follows. In Sec. II we describe the model used to simulate the erosion-deposition patterns. These patterns are presented

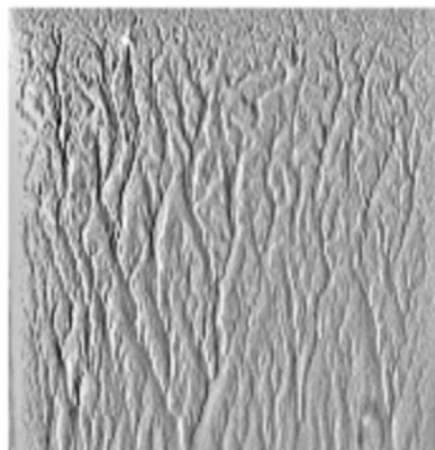


FIG. 1. Pattern observed in erosion experiment with commercial abrasive powder. Angles between  $30^\circ$  and  $90^\circ$  were found for different chevron alignments [14].

and analyzed in Sec. III, while the conclusions are left for Sec. IV.

## II. MODEL FORMULATION

We model a system that takes into account the interaction of a granular medium with an incompressible Newtonian fluid flowing through the corresponding pore space. The granular medium is initially considered as a  $N \times N$  regularized random network (RRN) on a horizontal plane where the sites are the centers of mass of spherical grains with diameter  $d$  that are totally submerged in a fluid (e.g., water). We initialize this network as a regular square where the distance between the closest neighbors is  $l_0$ . The points (centers of mass of the grains) are then moved randomly along vectors with arbitrary direction and random magnitude that are smaller than the distance between the points. In this way, the points are distributed randomly, but with a characteristic distance. More precisely, in order to avoid the occurrence of overlapping grains, the maximum value adopted for the modulus of these dislocation vectors is  $(l_0 - d)/2$ . The fluid flows in a direction parallel to the ground. Although the lattice construction is made in two dimensions (2D), we are actually describing one layer of a three-dimensional system, since the centers of mass of the particles still lie on a 2D plane, but the grains are considered to be spheres. This association will enable us to generate a network of capillaries representing a complex geometry of the pore space. At this point, the entire system is triangulated, considering each grain as a vertex of a Delaunay tessellation where the pore space is described by a Voronoi diagram. In Fig. 2 we show a typical initial RRN configuration and its corresponding triangulation and network of capillaries.

Next, we assume that the local pore geometry between each two nearest-neighbor grains  $i$  and  $j$  in this lattice can be modeled as a capillary channel of length  $l$  (the distance between the barycenters of the corresponding adjacent triangles), height  $d$ , and width  $w$  equal to the distance between their centers. As shown in Fig. 3, if we consider periodic boundary conditions (PBCs) in the  $x$  direction, such a channel should be equivalent to a parallelepiped of fluid containing in its center a solid sphere of diameter  $d$  (grain). Both planes describing the ground and the water/air interface of the lattice of particles are orthogonal to the  $y$  direction. Here the Navier-Stokes and continuity equations in the three-dimensional channel are solved using the commercial computational fluid dynamics (CFD) software FLUENT [23]. We consider no-slip boundary conditions at the bottom and assume that the top surface is shear-stress-free. A pressure gradient  $\Delta p$  is imposed between the two ends of the channel in the  $z$  direction. Its magnitude is sufficiently small to ensure viscous flow conditions, i.e., a low-Reynolds-number regime of flow. We adopt a nonstructured tetrahedral mesh to discretize the channel and an upwind finite-difference scheme is set to perform the numerical simulations. The steady-state velocity and pressure fields are calculated for different channel geometries by systematically varying the ratio  $w/d$  in the range  $1.0 < w/d < 10.0$ .

In Figs. 4(a)–4(c) we show three contour plots of the velocity field computed for a channel with porosity  $w/d$

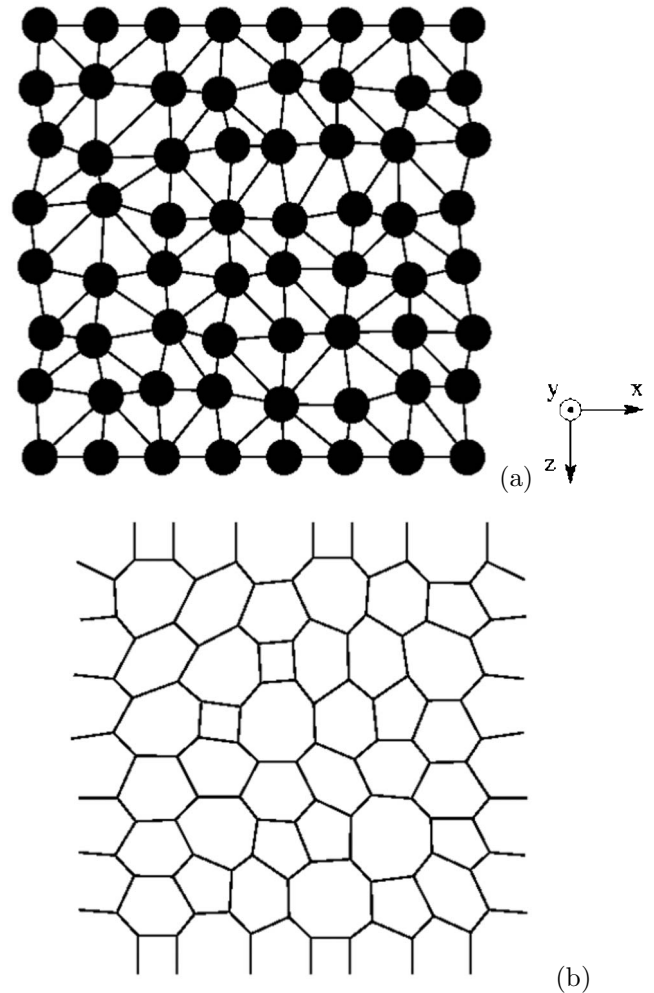


FIG. 2. Typical initial configuration of the regularized random network with 64 grains. In (a) we show its corresponding triangulation and in (b) its network of capillaries.

$= 1.05$  at heights  $y/d = 1/4$ ,  $1/2$ , and  $3/4$ , respectively. Considering the low-Reynolds-number conditions used in the simulations, the flow in the channel can be characterized in terms of a permeability index  $\kappa$  through the relation

$$v_f = - \frac{\kappa \Delta p}{\mu \Delta z}, \quad (1)$$

where  $\mu$  is the viscosity of the fluid and  $v_f$  is the average flow velocity. We assume that the movement of the particles does not transfer momentum to the flow field. Indeed, a more realistic approach would be to account for the momentum transfer from one phase to another, by adding the momentum change of every particle as it passes through a control volume of fluid. The exchange term would then appear as a sink in the continuous phase momentum balance [24,25]. Here a quasi-steady-state regime of flow is considered, i.e., the fluid flow adapts instantaneously to the porous medium geometry. This hypothesis should remain valid if inertial effects are not relevant. In practical terms, once the velocity and pressure fields are obtained for a channel with a given value of  $w/d$ , we can compute the mean velocity value  $v_f$  through a cross

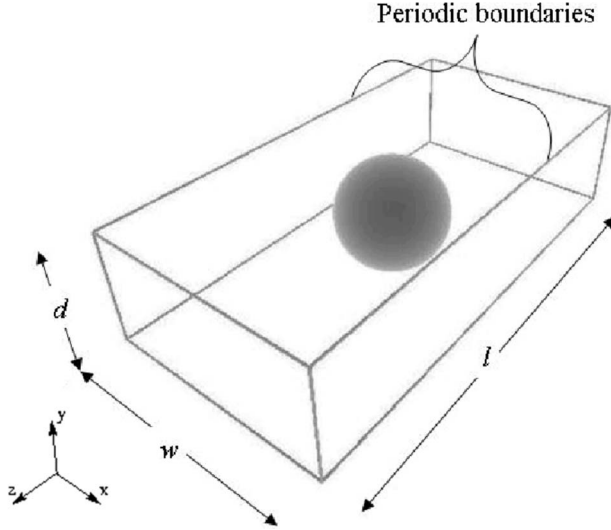


FIG. 3. Velocity field determined in a channel of length  $l$  and width  $w$  with one sphere of diameter  $d$  inside. The mean velocity of the fluid,  $v_f$ , is calculated in the rectangular cross section.

section orthogonal to the flow in the system. By repeating this procedure for different values of the overall pressure drop  $\Delta p$ , we first confirm the validity of the linear relationship  $v_f \propto \Delta p$  as expected from Eq. (1), so that the permeability  $\kappa$  can be directly calculated from the slope of the corresponding straight line. As shown in Fig. 5, the dependence of  $\kappa$  on the ratio  $w/d$  can be fully described as  $\kappa/\kappa_0 = f(w/d)$  where  $f(w/d)$  is a fourth-degree polynomial of  $w/d$  and  $\kappa_0$  is the permeability for a channel with unitary aspect ratio,  $w/d=1$ .

Once the local geometry and permeability of all capillaries in the system are determined, we proceed by applying a

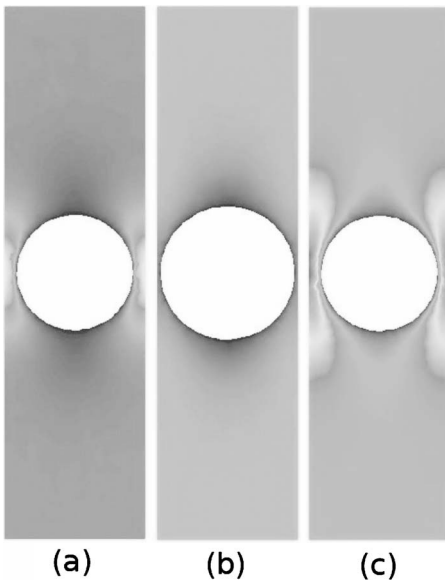


FIG. 4. Contour plots of the velocity field obtained numerically for  $w/d=1.05$  at three different transverse planes of the channel, namely,  $y/d=1/4$  (a),  $1/2$  (b), and  $3/4$  (c). The gray shades ranging from dark to light correspond to low- and high-velocity magnitudes, respectively.

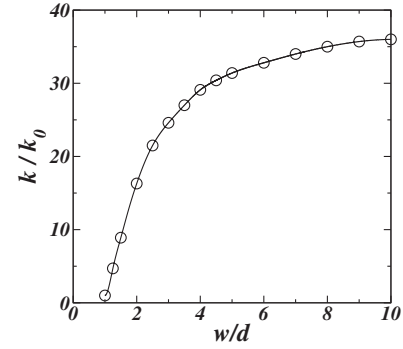


FIG. 5. Permeability  $\kappa$  versus the ratio  $w/d$  for the local channel configuration shown in Fig. 3. Here  $\kappa_0$  is the permeability for a channel with ratio  $w/d=1$ . The solid line is the best cubic spline interpolation to the data used to obtain the local permeability of the channels in the pore network model.

constant pressure drop between the inlet and outlet, i.e., the top and bottom of the entire pore network. Periodic boundary conditions are assumed in the lateral direction of the network, and the following local mass conservation equations are imposed at each of their  $N'$  nodes to allow water flow throughout the entire pore space:

$$\sum_j g_{ij}(p_i - p_j) = 0 \quad \text{for } i = 1, 2, \dots, N', \quad (2)$$

where the index  $j$  runs over all the neighbor nodes of node  $i$ ,  $g_{ij} \equiv wd\kappa/l$  is the hydraulic conductance in the capillary between the pores  $i$  and  $j$ , and  $p_i$  and  $p_j$  are the pressures at nodes  $i$  and  $j$ , respectively. Equation (2) corresponds to a set of  $N'$  coupled linear algebraic equations, where  $N'$  is the number of nodes in the system that can vary, depending on the configuration of the grains. These equations are solved in terms of the nodal pressure field by means of a standard subroutine for sparse matrices. From the pressures in the nodes, the velocity magnitude of the fluid in each capillary can be computed.

After the velocity field in the pore network is calculated, we allow each grain to move in the system. By assuming that there is no friction on the ground and drag is the only relevant force acting on the particles, we obtain

$$m \frac{d^2 \mathbf{x}}{dt^2} = 3\pi\mu d \sum_i (\mathbf{v}_f^i - \mathbf{v}), \quad (3)$$

where  $\mathbf{v}_f^i$  is the fluid velocity at the channel  $i$ ,  $\mathbf{v}$  is the particle velocity, and the vectorial sum on the right is taken over all  $n$  channels surrounding the particle. By straightforward integration of the equation of motion (3), the velocity and displacement caused by the fluid drag for each grain in the system during a time interval  $\Delta t$  can be written as

$$\mathbf{v} = \bar{\mathbf{v}}_f - (\bar{\mathbf{v}}_f - \mathbf{v}_0) e^{-nC\Delta t}, \quad (4)$$

$$\Delta \mathbf{x} = \bar{\mathbf{v}}_f \Delta t + (\bar{\mathbf{v}}_f - \mathbf{v}_0) \left( \frac{e^{-nC\Delta t} - 1}{nC} \right), \quad (5)$$

where  $\bar{\mathbf{v}}_f = \sum_i \mathbf{v}_f^i / n$ ,  $C = 18\mu / \rho d^2$ ,  $\rho = 6m / \pi d^3$  is the density of the grain, and  $\mathbf{v}_0$  is its velocity in the previous time step.

In our simulations, the center of each grain is displaced by  $\Delta x$  using a time step  $\Delta t$  that is sufficiently small to numerically ensure that the pattern evolution remains invariant when compared with results performed using even smaller time steps. The distance between the top and bottom lines of the system is kept constant, and each grain that goes out of the region delimited by these lines is replaced by another grain at the top of the lattice. What is crucial for the steadiness of the pattern formation is that one grain cannot overlap with another grain. After computing the movement of all grains at each time step, the pore space is then modified, and we repeat the calculation of the velocity field to move the grains again, and so on. The simulation stops when the system reaches the steady state, i.e., when the geometry of the aggregate remains unchanged with time.

### III. RESULTS

We performed simulations on a lattice with  $32 \times 32$  grains with diameter  $d=30 \mu\text{m}$  and density  $\rho=2.75 \text{ g/cm}^3$ . These particles are surrounded by water, i.e., a fluid of viscosity  $\mu=10^{-3} \text{ Pa s}$  which flows at small-Reynolds-number conditions ( $\text{Re} \ll 1$ ) through a pore space of porosity that can be varied in the range  $0.48 < \phi < 0.8$ . For each value of porosity we obtain results for five different realizations of the initial random pore space.

In Figs. 6(a)–6(c) we show three final stable configurations of the model for different porosity values  $\phi=0.57$ , 0.71, and 0.80, respectively. As can be observed, the steady-state patterns depend strongly on the porosity of the system. For sufficiently large values of  $\phi$ , the occurrence of particle clusters in the form of dendrites reflects the strong coupling between fluid dynamics and grain movement, where the aligned preferential channels for flow leads to a high overall permeability of the porous system. For small porosities, however, no characteristic pattern is observed. This is to be expected since in compacted systems the grains do not have much mobility, while in loose systems the particles have the freedom to move in almost all directions. The tendency to form a dendritic pattern in which the particles align in preferential directions can be statistically quantified if we determine for each pair of grains the angle  $\alpha$  between the line connecting their centers of mass and the direction orthogonal to the flow [i.e., the  $x$  direction shown in Fig. 6(a)]. In Figs. 7(a)–7(c) we show the histograms of these angles,  $N(\alpha)$ , for  $\phi=0.57$ , 0.71, and 0.80. For a low-porosity system,  $\phi=0.57$ , the results shown in Fig. 7(a) indicate that a significant number of grains are aligned around  $\alpha=25^\circ$  (and the symmetric direction of  $155^\circ$ ), although the most frequent angle lies in the vicinity of  $90^\circ$ . This means that the particles tend to be aligned in the vertical  $y$  direction (i.e., the direction of the flux), what is expected as the system cannot change much from its initial configuration. In systems with intermediate porosity values,  $0.65 < \phi < 0.75$ , there is a substantial change in the preferred angle of alignment, which is around  $\alpha=60^\circ$  (and the symmetric direction of  $120^\circ$ ). This behavior, as exemplified here in Fig. 7(b), resembles the chevron alignment reported in Ref. [14], where the results of the angle histograms are presented for a porosity  $\phi=0.71$ . In

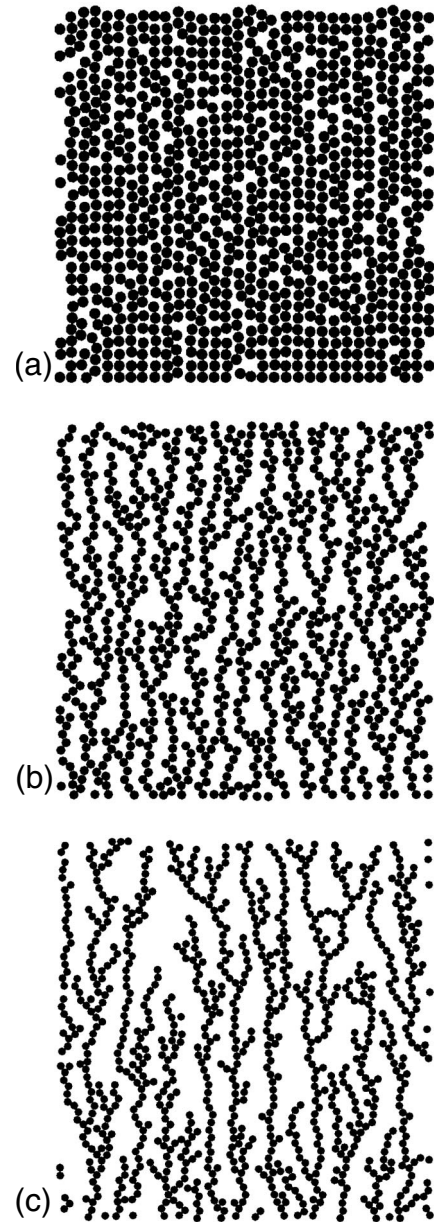


FIG. 6. Final configurations of the system for porosities  $\phi=0.57$  (a), 0.71 (b), and 0.80 (c) after 15 000 time steps. The grains arrange themselves in positions that give rise to characteristic patterns.

this reference, experimentally preferred angles around the same value were also found. In Fig. 7(c) we show the histogram  $N(\alpha)$  for a large-porosity system,  $\phi=0.80$ , where no evident preferential direction can be observed, with the particles aligning themselves at angles between  $50^\circ$  and  $130^\circ$  with approximately the same probability.

Finally, it is important to investigate the flow properties of the porous system in terms of its macroscopic permeability  $\kappa$  as a function of porosity. In Fig. 8 we show that the permeability increases with porosity for diluted systems (i.e., for low  $\phi$  values) and with high values of  $\phi$ . Interestingly, we find that this behavior can be well described by a power law function in the form  $\kappa/\kappa_0=a\phi^b$ , as also depicted in Fig. 8.

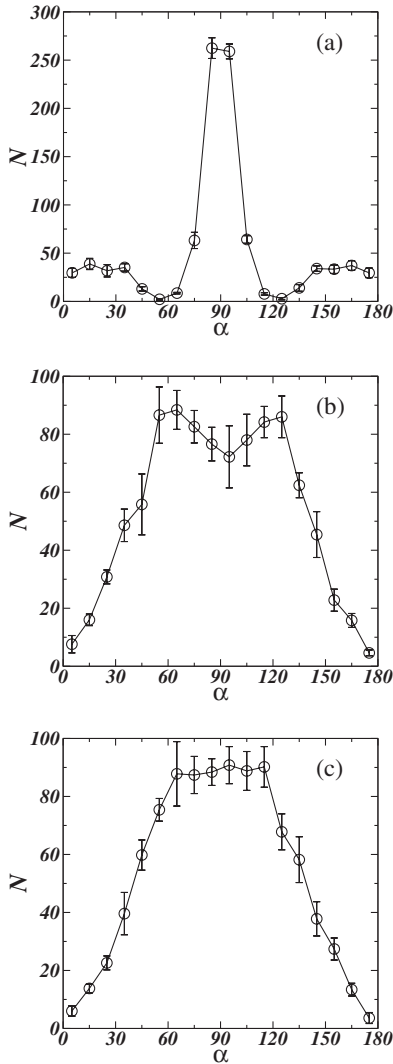


FIG. 7. Histograms of pairs of grains that are touching and for which the line joining their centers of mass forms an angle  $\alpha$  with the axis  $x$ . These results represent the average over five realizations of different porosities, namely,  $\phi =$  (a) 0.57, (b) 0.71, and (c) 0.80.

IV. CONCLUSIONS

We developed a numerical model to describe the process of erosion-deposition caused by laminar flow, with the drag force given by Stokes law. The results we obtained show the formation of a typical erosion pattern characterized by chevron alignments very similar to the experimental ones presented in Ref. [14] (a typical pattern is shown in Fig. 1). Through computational simulations performed with this model, we were able to find dendritic patterns as well as to reproduce the preferential alignment of the chevron structures observed in real experiments.

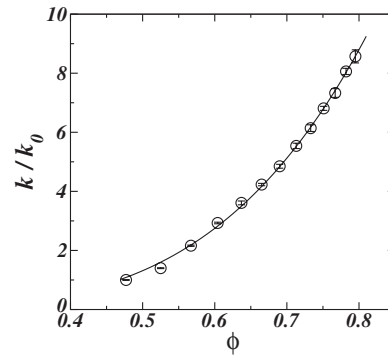


FIG. 8. Dependence of the macroscopic permeability  $\kappa$  at the steady state on the porosity  $\phi$  of the erosion-deposition system. The solid line is the best fit to the data of the function  $\kappa / \kappa_0 = a\phi^b$ , with parameters  $a = 21.5 \pm 0.5$  and  $b = 4.0 \pm 0.5$ .

Our results indicate that these patterns depend substantially on the porosity of the system. Previous studies [26–28] have shown that the size and shape of the particles dramatically influence the propagation of the fluid and the stress distribution in the system. In addition, it has been shown experimentally that the pattern geometry must also depend on the flow properties through the porous medium [29,30], namely, on whether or not the inertial mechanisms of momentum transport play an important role on the dynamics of pattern formation. In the present study we considered only laminar flow. By changing the exponent of the velocity in the drag law, for example, one can reproduce aspects of turbulent flow to increase the complexity in the movement of the particles. This could reveal a variety of new patterns. How the shape and the size distribution of the grains as well as the flow characteristics affect the patterns are natural questions that will be addressed in future work.

In recent works [16,18,31], many patterns were observed in experiments involving avalanches, where one of the most important parameters is the depth of the substrate. Although the system studied here is related to erosion-sedimentation processes, this suggests that a variety of different patterns may be obtained just when one attempts to simulate them in three dimensions. A simple approximation to a three-dimensional system would be to consider that, depending on the flux, a particle would not stop as it reaches another particle, but could jump over it. With this possibility, the dynamics of the particles changes, as their velocity now depends also on the height of their centers of mass.

ACKNOWLEDGMENTS

We appreciate helpful interactions with A. M. C. Souza, A. A. P. Olarte, A. A. Moreira, and S. McNamara. This work was supported by the Brazilian agencies CNPq, CAPES, and FUNCAP and Deutscher Akademischer Austauschdienst (DAAD). H. J. Herrmann thanks the Max-Planck Foundation.

- [1] R. Behringer, H. Jaeger, and S. Nagel, *Chaos* **9**, 509 (1999).
- [2] H. M. Jaeger, S. R. Nagel, and R. P. Behringer, *Rev. Mod. Phys.* **68**, 1259 (1996).
- [3] P. S. Dodds and D. H. Rothman, *Annu. Rev. Earth Planet. Sci.* **28**, 571 (2000).
- [4] B. F. Edwards and D. H. Smith, *Phys. Rev. E* **65**, 046303 (2002).
- [5] H. J. Herrmann, G. Sauer mann, and V. Schwämmle, *Physica A* **358**, 30 (2005).
- [6] O. Durán and H. J. Herrmann, *Phys. Rev. Lett.* **97**, 188001 (2006).
- [7] S. Krishnamurthy, V. Loreto, H. J. Herrmann, and S. Roux, *Physica A* **270**, 89 (1999).
- [8] Y. Grasselli and H. J. Herrmann, *Physica A* **246**, 301 (1997).
- [9] A. Betat, V. Frette, and I. Rehberg, *Phys. Rev. Lett.* **83**, 88 (1999).
- [10] K. Kroy, G. Sauer mann, and H. J. Herrmann, *Phys. Rev. Lett.* **88**, 054301 (2002).
- [11] H. J. Herrmann, *Physica A* **263**, 51 (1999).
- [12] D. Ertas and T. C. Halsey, *Europhys. Lett.* **60**, 931 (2002).
- [13] H. Seybold, J. S. Andrade, and H. J. Herrmann, *Proc. Natl. Acad. Sci. U.S.A.* **104**, 16804 (2007).
- [14] A. Daerr, P. Lee, J. Lanuza, and E. Clement, *Phys. Rev. E* **67**, 065201(R) (2003).
- [15] O. Pouliquen, *Phys. Fluids* **11**, 542 (1999).
- [16] I. S. Aranson, F. Malloggi, and E. Clement, *Phys. Rev. E* **73**, 050302(R) (2006).
- [17] O. Pouliquen and J. W. Vallance, *Chaos* **9**, 621 (1999).
- [18] T. Borzsonyi, T. C. Halsey, and R. E. Ecke, *Phys. Rev. Lett.* **94**, 208001 (2005).
- [19] Y. Forterre and O. Pouliquen, *J. Fluid Mech.* **486**, 21 (2003).
- [20] O. Pouliquen, *Phys. Rev. Lett.* **93**, 248001 (2004).
- [21] G. D. R. Midi, *Eur. Phys. J. E* **14**, 341 (2004).
- [22] O. Pouliquen, J. Delour, and S. B. Savage, *Nature (London)* **386**, 816 (1997).
- [23] The FLUENT fluid dynamics analysis package has been used in this study; <http://www.fluent.com>
- [24] O. Johnsen, R. Toussaint, K. J. Maloy, and E. G. Flekkoy, *Phys. Rev. E* **74**, 011301 (2006).
- [25] S. McNamara, E. G. Flekkoy, and K. J. Maloy, *Phys. Rev. E* **61**, 4054 (2000).
- [26] J. Geng, D. Howell, E. Longhi, R. P. Behringer, G. Reydellet, L. Vanel, E. Clement, and S. Luding, *Phys. Rev. Lett.* **87**, 035506 (2001).
- [27] G. Reydellet and E. Clement, *Phys. Rev. Lett.* **86**, 3308 (2001).
- [28] G. W. Baxter, R. P. Behringer, T. Fagert, and G. A. Johnson, *Phys. Rev. Lett.* **62**, 2825 (1989).
- [29] J. S. Andrade, D. A. Street, T. Shinohara, Y. Shibusa, and Y. Arai, *Phys. Rev. E* **51**, 5725 (1995).
- [30] J. S. Andrade, U. M. S. Costa, M. P. Almeida, H. A. Makse, and H. E. Stanley, *Phys. Rev. Lett.* **82**, 5249 (1999).
- [31] F. Malloggi, J. Lanuza, B. Andreotti, and E. Clement, *Europhys. Lett.* **75**, 825 (2006).